Automated design methodology of turbulent internal flow using discrete adjoint formulation

Byung Joon Lee [a,1], Chongam Kim [b,*,2]

[a] *School of Mechanical and Aerospace Engineering, Seoul National University, 151-744, Seoul, Republic of Korea*
[b] *Institute of Advanced Aerospace Technology, Seoul National University, Republic of Korea*

Abstract

An optimal shape design approach is presented for a subsonic S-shaped intake geometry using aerodynamic sensitivity analysis. Sensitivity analysis is performed for the three-dimensional Navier–Stokes equations coupled with two-equation turbulence models using a discrete adjoint method. For code validation, the result of the flow solver is compared with experimental data and other computational results. Through the study on turbulence models and grid refinement, results from several turbulence models are compared and the minimal number of grid points yielding an accurate numerical solution is obtained. And, the adjoint sensitivity code is also validated by the comparison with complex step derivative results. To obtain a sufficient and flexible design space, NURBS equations are employed as a geometric representation and a new grid modification technique, Least Square NURBS Grid Approximation is applied. With the verified flow solver, sensitivity analysis code and geometric modification technique, the optimization of the S-shaped intake is carried out and the enhancement of overall intake performance is achieved. In addition, the off-design performance of a designed S-shaped intake is tested to confirm the robustness of the current design approach. As a result, the capability and efficiency of the present design tools are successfully demonstrated in three-dimensional high Reynolds subsonic intake design.
© 2006 Elsevier Masson SAS. All rights reserved.

Keywords: Adjoint approach; Aerodynamic shape optimization; NURBS approximation; Internal flow design

1. Introduction

Both commercial and military aircrafts generally adopt S-shaped ducts to deliver the captured flow from the far field into engine compressor. Engine efficiency is greatly influenced by intake performance. Thus, an inlet duct should be designed to deliver uniform and high pressure-recovery flow to the engine face.

In order to increase aircraft pay-load and reduce energy loss, inlet length should be as short as possible. Short inlet length, however, entails high curvature in duct shape which may cause massively separated flows. Thus, in order to design a high-performance intake, it is one of the most important problems to find an optimal trade-off between geometric constraint and flow delivery performance. Intake performance is generally determined by: (1) incoming flow angularity with respect to the inlet cowl lip, (2) uniform and high pressure-recovery flow at the engine face, (3) vortex, wake and boundary layer ingestion by the inlet, (4) interference between the flows generated by the other parts of aircraft and ingested flow at the inlet. These performances are measured by various performance coefficients such as total pressure recovery, swirling coefficient, engine face distortion coefficient (DC), average circumferential distortion descriptor (DPCP), maximum radial distortion descriptor (DPRP$_{mx}$), and so on. Among the performance factors, many precedent experimental and computational research treated engine face distortion and total pressure recovery as the most critical indexes in intake design [1,24,25]. Engine face distortion represents the degree of flow non-uniformity at the engine face. Non-uniform flow at the engine face is generated by several factors such as disturbances by fuselage and/or lip

* Corresponding author.
  E-mail address: chongam@snu.ac.kr (C. Kim).
[1] Ph.D. Candidate, Department of Aerospace Engineering.
[2] Associate Professor, Department of Aerospace Engineering.

effect, secondary flow or flow separation inside the duct itself. And these factors cause total pressure loss, too [22]. Thus, an optimal shape design of an S-shaped intake should alleviate or remove the detrimental factors and, as a result, make the flow at the engine face more uniform with less energy loss.

With regard to flow analysis, previous research focused on an accurate prediction of flow separation in the S-shaped duct with more refined grid systems and/or more suitable turbulence models. And it is concluded that two-equation turbulence models predict the duct flow better than algebraic and one-equation models [6,19,21,23,26]. In the present work, flow analysis results from several turbulence models are compared. And, a grid refinement study is carried out with various sizes of grid systems. Especially, for the ultimate goal of the present work, i.e., the optimal shape design of engine intake, both efficiency and accuracy of the flow solver are carefully investigated on a coarse grid system below the level of 300,000 grid points.

Tremendous progress has been achieved in the area of ASO (Aerodynamic Shape Optimization) such as airfoil and wing/body design in transonic flow regime. For a large number of design variables, GBOM (Gradient Based Optimization Method) using adjoint approach is very popular because of its computational efficiency [3,4,11,15,20]. For an accurate prediction of the separated flow in a duct, two-equation turbulence models are very appealing in both the flow analysis and the sensitivity analysis though its computational cost is somewhat burdensome [14]. In the design optimization field, adjoint approach which has been very successful in external flow problems does not seem to be applied to highly viscous internal flow problems yet. This is mainly due to the difficulty in differentiating turbulence transport equations [9]. In addition, awfully time consuming work in developing a reliable adjoint code may discourage its application to duct design problems. For these reasons, numerous research on optimal intake design employs parametric studies, GBOM using finite difference method, or other global optimization method based on the modeling of design space. Unfortunately, these approaches only provide local shape modification rather than global shape design because of computational inefficiency for a large number of design variables [24,25,28]. Undoubtedly, flow control devices such as Gaussian bump, vortex generating vanes/jets substantially improve overall flow quality. Especially, the vortex generator devised by Gibb et al. is a very efficient device to control separated flow and to maintain high flow quality at the engine face [1]. However, these works are focused on the determination of the position and geometry of a flow control device, not on the design optimization of duct shape itself. In the present work, we carry out the design optimization of a duct shape based on the adjoint approach. Sensitivity analysis for two-equation turbulence model is performed to allow a large number of design variables and to globally modify the duct geometry. The computational cost caused by two adjoint equations for turbulence transport equations is side-stepped by the parallelized AV method [13]. As a result, the computational cost of one sensitivity analysis with the parallelized AV method is almost equal to that of the flow solver. Sensitivity analysis

results are validated by comparing complex step derivative results [16].

A flexible geometric representation is another critical requirement for an automated shape design methodology. Geometric representation techniques based on the superposition of local shape functions, such as Hicks–Henne functions or Chebyshev polynomial, are widely used in transonic wing/body design because it maintains the smoothness of airfoil shape [7, 9,13]. These methods, however, are not suitable to provide a sufficient and flexible design space in case of 3-dimensional or 2-dimensional problems if geometric change is severe. All surface grid points may be used as design variables but surface grids are naturally discontinuous. Thus, the perturbation of each grid point may not be able to guarantee the smoothness of modified grid. As a result, some additional process such as gradient smoothing is essential [8,15]. In addition, unlike conventional external aerodynamic design problems where small grid perturbation may eliminate shocks on wing surface, substantial geometric variation is inevitable in S-shaped duct design [14]. For these reasons, a NURBS (Non-Uniform Rational B-Spline) equation is employed as a new shape function in the present work and the control points of NURBS surface are used as design variables. NURBS can express any shape change on the duct surface and the degrees of freedom for the design space can be determined flexibly. Simultaneously, NURBS can maintain grid smoothness since NURBS equations can preserve a certain level of higher order derivatives at each knot of surface. Hence, gradient smoothing which affects the accuracy of the sensitivity is no longer necessary.

Exploiting those techniques, several cases of intake design are carried out in this work. The objective function is a weighted combination of total pressure recovery, distortion, and inlet mass flow rate. In a subsonic intake, a change in flow pattern may affect mass flow rate at inlet. Thus, mass flow rate is incorporated into the objective function in the form of a penalty function. Finally, example design problems for the maximization of total pressure recovery and the minimization of distortion maintaining a mass flow rate condition are performed to evaluate the performance of the present automatic design approach.

2. Numerical background

For the aerodynamic shape optimization with a gradient-based approach, 4 modules are combined, i.e., flow analysis code, sensitivity analysis code based on an adjoint approach, NURBS approximation code for flexible grid deformation, and optimization algorithm. In order to reduce computing time, both the flow solver and the sensitivity analysis codes are parallelized using MPI (Message Passing Interface) programming. Numerical methods are summarized in Table 1.

2.1. Flow analysis code

The governing equations are the three-dimensional compressible Navier–Stokes equations coupled with the k–ω SST turbulence model [18]. The governing equations are transformed to generalized coordinates and are solved with a finite-

Table 1
Numerical methods for the flow solver & design optimization

		Numerical methods
Flow solver	Governing equations	3-D compressible RANS
	Flux function	RoeM[24]
	Higher order interpolation	MUSCL (3rd order)
	Viscous flux	Central difference
	Time integration	LU-SGS
	Turbulence model	kw-SST
	Parallelization library	MPI
Sensitivity analysis		Discrete adjoint method (Full N–S equations with kw-SST model)
Geometric representation		Least square NURBS approximation
Optimizer		BFGS (Broyden–Fletcher–Goldfarb–Shanno)

volume method. For the calculation of the residual, convective terms are upwind-differenced based on RoeM scheme by Kim et al. [10] and viscous terms are central-differenced. A MUSCL (Monotone Upstream Centered Scheme for Conservation Laws) approach using a third order interpolation is used to obtain a higher order of spatial accuracy in all calculations. For temporal integration, Yoon's LU-SGS scheme is applied [27].

2.2. Sensitivity analysis code

The discrete adjoint approach is applied to obtain sensitivity information and the three-dimensional Navier–Stokes equations coupled with two-equation turbulence models are fully hand-differentiated. The discrete residual of the steady-state flow equations can be written as

$$\{R\} = \big\{R(Q, X, \beta_k)\big\} = \{0\}, \tag{1}$$

where Q is the flow variable vector, X is the computational grid position and β_k is the vector of design variables. Similarly, the aerodynamic objective function F to be either minimized or maximized is also dependent on Q, X and β_k as

$$\{F\} = \big\{F(Q, X, \beta_k)\big\}. \tag{2}$$

The sensitivity derivatives of the aerodynamic function are calculated by directly differentiating Eqs. (1) and (2) with respect to β_k as

$$\left\{\frac{\mathrm{d}R}{\mathrm{d}D}\right\} = \left[\frac{\partial R}{\partial Q}\right]\left\{\frac{\mathrm{d}Q}{\mathrm{d}\beta_k}\right\} + \left[\frac{\partial R}{\partial X}\right]\left\{\frac{\mathrm{d}X}{\mathrm{d}\beta_k}\right\} + \left\{\frac{\partial R}{\partial \beta_k}\right\} = \{0\}, \tag{3}$$

$$\left\{\frac{\mathrm{d}F}{\mathrm{d}\beta_k}\right\} = \left\{\frac{\partial F}{\partial Q}\right\}^{\mathrm{T}}\left\{\frac{\mathrm{d}Q}{\mathrm{d}\beta_k}\right\} + \left\{\frac{\partial F}{\partial X}\right\}^{\mathrm{T}}\left\{\frac{\mathrm{d}X}{\mathrm{d}\beta_k}\right\} + \left\{\frac{\partial F}{\partial \beta_k}\right\}. \tag{4}$$

Efficient evaluation of $\{\partial Q/\partial \beta_k\}$ from Eq. (4) is essential in problems involving many design variables. In adjoint approach, the sensitivity derivatives of the aerodynamic function are obtained by combining Eq. (3) with Eq. (4) as

$$\left\{\frac{\mathrm{d}F}{\mathrm{d}\beta_k}\right\} = \left\{\frac{\partial F}{\partial Q}\right\}^{\mathrm{T}}\left\{\frac{\mathrm{d}Q}{\mathrm{d}\beta_k}\right\} + \left\{\frac{\partial F}{\partial X}\right\}^{\mathrm{T}}\left\{\frac{\mathrm{d}X}{\mathrm{d}\beta_k}\right\} + \left\{\frac{\partial F}{\partial \beta_k}\right\}$$
$$+ \Lambda^{\mathrm{T}}\left(\left[\frac{\partial R}{\partial Q}\right]\left\{\frac{\mathrm{d}Q}{\mathrm{d}\beta_k}\right\} + \left[\frac{\partial R}{\partial X}\right]\left\{\frac{\mathrm{d}X}{\mathrm{d}\beta_k}\right\} + \left\{\frac{\partial R}{\partial \beta_k}\right\}\right), \tag{5}$$

where Λ represents the 7-element adjoint variable vector. Rearranging Eq. (5) yields the following equation.

$$\left\{\frac{\mathrm{d}F}{\mathrm{d}\beta_k}\right\} = \left\{\frac{\partial F}{\partial X}\right\}^{\mathrm{T}}\left\{\frac{\mathrm{d}X}{\mathrm{d}\beta_k}\right\} + \left\{\frac{\partial F}{\partial \beta_k}\right\}$$
$$+ \Lambda^{\mathrm{T}}\left(\left[\frac{\partial R}{\partial X}\right]\left\{\frac{\mathrm{d}X}{\mathrm{d}\beta_k}\right\} + \left\{\frac{\partial R}{\partial \beta_k}\right\}\right)$$
$$+ \left(\left\{\frac{\partial F}{\partial Q}\right\}^{\mathrm{T}} + \Lambda^{\mathrm{T}}\left[\frac{\partial R}{\partial Q}\right]\right)\left\{\frac{\mathrm{d}Q}{\mathrm{d}\beta_k}\right\}. \tag{6}$$

Without evaluating the vector $\{\partial Q/\partial \beta_k\}$, the sensitivity derivatives of the aerodynamic function can be calculated as

$$\left\{\frac{\mathrm{d}F}{\mathrm{d}\beta_k}\right\} = \left\{\frac{\partial F}{\partial X}\right\}^{\mathrm{T}}\left\{\frac{\mathrm{d}X}{\mathrm{d}\beta_k}\right\} + \left\{\frac{\partial F}{\partial \beta_k}\right\}$$
$$+ \Lambda^{\mathrm{T}}\left(\left[\frac{\partial R}{\partial X}\right]\left\{\frac{\mathrm{d}X}{\mathrm{d}\beta_k}\right\} + \left\{\frac{\partial R}{\partial \beta_k}\right\}\right), \tag{7}$$

if and only if the adjoint vector Λ satisfies the following adjoint equation.

$$\left[\frac{\partial R}{\partial Q}\right]^{\mathrm{T}}\Lambda + \left\{\frac{\partial F}{\partial Q}\right\} = \{0\}^{\mathrm{T}}. \tag{8}$$

The solution vector Λ is obtained by the implicit Euler method of Eq. (8) as

$$\left(\frac{I}{J\Delta t} + \left[\frac{\partial R}{\partial Q}\right]^{\mathrm{T}}_{VL}\right)\Delta\Lambda = -\left[\frac{\partial R}{\partial Q}\right]^{\mathrm{T}}\Lambda^m - \left\{\frac{\partial F}{\partial Q}\right\}^{\mathrm{T}},$$
$$\Lambda^{m+1} = \Lambda^m + \Delta\Lambda. \tag{9}$$

Here, the matrix I indicates an identity matrix and J is Jacobian. The van-Leer flux Jacobian which is conventionally used in the flow solver is indicated by $[\partial R/\partial Q]^{\mathrm{T}}_{VL}$ in order to distinguish it from the flux Jacobian of the adjoint equation, $[\partial R/\partial Q]^{\mathrm{T}}$. The overall procedure is also described in the Ref. [9].

This approach can provide the computational cost of the sensitivity independent on the number of design variables while maintaining the level of accuracy up to the third or fourth decimal place compared with the results of complex step derivative.

The complex step derivative method is devised by J. Martins et al. [16]. The sensitivity of an objective function, F, with respect to a geometric variable, x, can be evaluated by the complex form as

$$\frac{\mathrm{d}F}{\mathrm{d}x} = \frac{\mathrm{Im}(F(x + i\Delta x))}{\Delta x}. \tag{10}$$

By the Taylor series expansion for the objective function, F,

$$F(x + i\Delta x) = F(x) + i\frac{\mathrm{d}F(x)}{\mathrm{d}x}\Delta x - \frac{\mathrm{d}^2 F(x)}{\mathrm{d}^2 x}\frac{\Delta x^2}{2!}$$
$$- i\frac{\mathrm{d}^3 F(x)}{\mathrm{d}^3 x}\frac{\Delta x^3}{3!} + \cdots, \tag{11}$$

the imaginary part of Eq. (10) is obtained and the first order derivative, $\mathrm{d}F/\mathrm{d}x$, can be represented by

$$\mathrm{Im}\big(F(x + i\Delta x)\big) = \frac{\mathrm{d}F(x)}{\mathrm{d}x}\Delta x + \mathrm{O}(\Delta x^3). \tag{12}$$

Then the sensitivity can be evaluated with the error lower than $O(\Delta x^3)$. If the step size of perturbation is less than 10^{-6}, the error of complex step derivative can decrease to the level of machine accuracy. For more elaborate derivation process, refer [16].

2.3. Least square NURBS grid approximation

In automatic shape design for three-dimensional geometry, a grid generator which guarantees a sufficient and flexible design space is extremely important. In the present work, NURBS (Non-Uniform Rational B-Spline) surface equations are employed as new shape functions. The benefits of NURBS have already been mentioned in the previous section. In this section, the determination of control points and NURBS blending functions, grid generation process from the evaluated NURBS equations are presented. The coordinate vectors of NURBS curve, $X(u)$, are expressed by

$$X(u) = \frac{\sum_{i=0}^{n} h_i P_i N_{i,k}(u)}{h}, \tag{13}$$

where homogeneous coordinate h represents

$$h = \sum_{i=0}^{n} h_i N_{i,k}(u), \tag{14}$$

and $P_i = (x_i, y_i, z_i)$ is a position vector of the ith control point in three-dimensional space. Homogeneous coordinates play a role of weighting factor for each control point. As the value of h increases, the corresponding NURBS curve is closer to the control point. In the present approximation, all the homogeneous coordinates are set to 1 to impose equal weighting for each control point. The value of n indicates the number of control points. Also, blending functions are defined as

$$N_{i,k}(u) = \frac{(u - t_i)N_{i,k-1}(u)}{t_{i+k} - t_i} + \frac{(t_{i+k+1} - u)N_{i+1,k-1}(u)}{t_{i+k+1} - t_{i+1}},$$
$$N_{i,0}(u) = \begin{cases} 1 & (t_i \leqslant u \leqslant t_{i+1}), \\ 0 & (\text{otherwise}), \end{cases} \tag{15}$$

where t_i ($i = 0, 1, 2, \ldots$) are knot-values, and subscript k indicates the order of NURBS blending function [12].

Generally, there are two ways of constructing a NURBS curve, NURBS interpolation and NURBS approximation. In case of a NURBS interpolation scheme [12,21], the number of acquired control points, $n + 1$, is the same as the number of grid points, $m + 1$. In other words, each evaluated control points can alter only one grid point. As a result, the discontinuous nature of grid point distribution may cause problems in the design process and the benefit of NURBS equations in maintaining high smoothness may disappear. In order to support the smoothness of modified grid surface and curve, the number of evaluated control point should be less than the number of grid point.

Therefore, NURBS interpolation is not suitable for grid modification in ASO. In the present study, control points P_i for design variables and blending functions $N_{i,k}(u)$ of the duct surface are evaluated from a least squares NURBS approximation. The process of NURBS approximation is to reproduce

a polynomial curve equation by the kth order approximation, which passes through the given $m + 1$ surface grid points of the baseline model, $\mathbf{Q_0}, \ldots, \mathbf{Q_m}$ ($m > n$, $1 \leqslant k \leqslant n$). Needless to say, the approximation may possess some degree of inaccuracy in the shape representation. However, inaccuracy due to the approximated curve equation can be avoided by introducing a sufficient number of control points. By specifying the number of control points, a designer can control the accuracy in flow analysis and/or the range of design space in the design optimization.

In a least square NURBS approximation, the parameter $\bar{u}_i$ is evaluated by the distance ratio between grid points as shown in Eq. (16) to maintain the initial grid distribution.

$$\bar{u}_i = \bar{u}_{i-1} + \frac{|\mathbf{Q}_i - \mathbf{Q}_{i-1}|}{d}, \quad i = 1, \ldots, n-1,$$
$$d = \sum_{i=1}^{n} |\mathbf{Q}_i - \mathbf{Q}_{i-1}|, \tag{16}$$

with $\bar{u}_0 = 0$, $\bar{u}_n = 1$. And, knots are calculated such that every knot span should contain at least one $\bar{u}_i$.

Let

$$\kappa = \frac{m+1}{n-k+1}, \quad i = \text{int}(j\kappa), \quad \alpha = j\kappa - i. \tag{17}$$

Then internal knots can be defined by

$$t_{k+j} = (1 - \alpha)\bar{u}_{i-1} + \alpha\bar{u}_i \tag{18}$$

with $j = 1, \ldots, n - k$.

And then, the kth order non-rational curve in the form of Eq. (13) is determined such that it satisfies

1) $\mathbf{Q}_0 = X(0)$, $\mathbf{Q}_m = X(1)$.

2) The remaining $\mathbf{Q}_i$ are approximated in the least square sense, i.e.,

$$\sum_{i=1}^{m-1} |\mathbf{Q}_i - X(\bar{u}_i)|^2 \tag{19}$$

is minimized with respect to the $n + 1$ variables, P_i. Then, control points P_i and blending functions $N_{i,k}(u)$ for NURBS equations are finally determined. For more details, refer Chapter 9 of Ref. [21].

After this process, control points and homogeneous coordinates (weighting factors) can be used as design variables. And, grid sensitivity is finally evaluated as in Eqs. (20), (21).

For the ith control point,

$$\frac{\partial X(u)}{\partial P_i} = \frac{h_i N_{i,k}(u)}{\sum_{i=0}^{n} h_i N_{i,k}(u)}. \tag{20}$$

And, for the ith weighting factor,

$$\frac{\partial X(u)}{\partial h_i} = \frac{N_{i,k}(u)\left[\sum_{j=0}^{n}\{(P_i - P_j)h_j N_{j,k}(u)\}\right]}{\left[\sum_{j=0}^{n} h_j N_{j,k}(u)\right]^2}. \tag{21}$$

In case of a NURBS surface approximation, the overall procedure is similar to a NURBS curve approximation except it is formulated by two-dimensional NURBS equations. Volume grids are made from section grids along the duct centerline direction. The wall boundary of each section is provided by
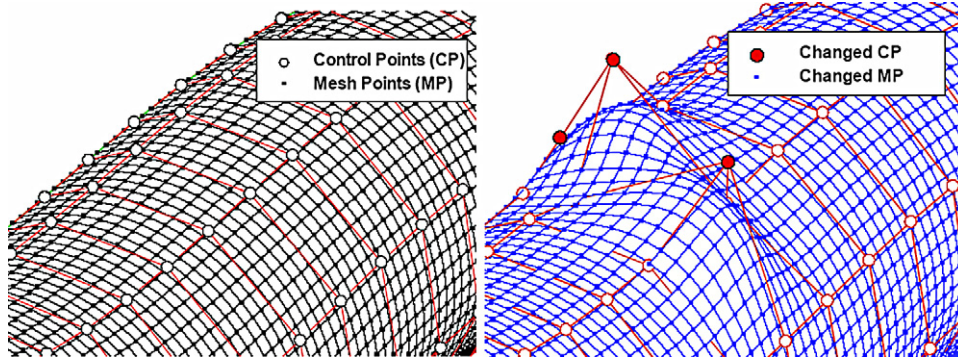
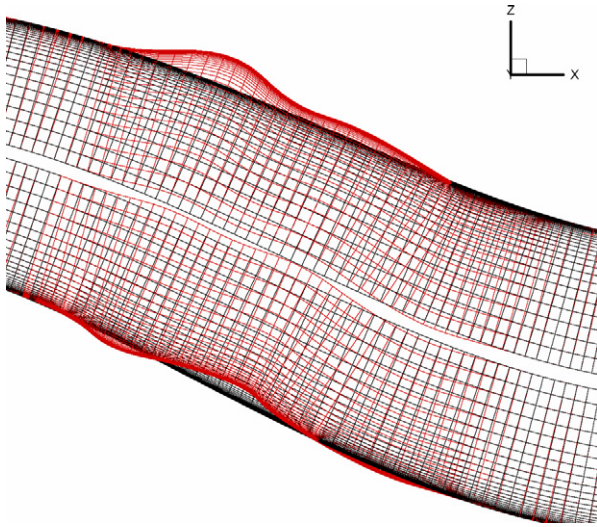Fig. 1. NURBS surface and control points for S-shaped duct.

Fig. 2. Surface modification using approximated NURBS function.

Fig. 3. Geometric information of RAE2129 intake.

approximated surface grids, and section grids can be generated by interpolating centerline grids and surface grids. Because the sensitivities of inner volume grids can be represented by NURBS blending functions, weighting factor and control points, grid sensitivities are obtained analytically by differentiating algebraic functions.

Fig. 1 shows the approximated duct surface. High-quality surface grids can be seen. Dot points on surface grids indicate control points. In Fig. 2, modified surface and volume grids are presented. Although the geometric change is not realistic, it shows a very high flexibility in shape modification.

3. Flow analysis & validation

3.1. Test model

Flow analysis results are benchmarked by experimental data and computational results for the 3.1 case of AGARD AR-270 [5]. Flow condition for the present design work is given by the free stream Mach number of 0.21 and the Reynolds number of 7,770,000 based on the diameter of throat. Although the free-stream Mach number is relatively small, a high mass flow rate yields high transonic flow inside the duct due to flow acceleration at intake entrance. Additionally, the results of the

present flow solver under different throat Mach number conditions are compared with the DRA experimental data by varying the back pressure at the outlet boundary of the duct [1]. The duct geometry is the RAE2129 intake, which is a test model in the AGARD paper [5,19]. The present configuration of the S-shaped subsonic diffuser is specified by the equations of duct centerline and radius at each section as shown in Fig. 3 [23]. Geometric representations are given by Eqs. (22), (23). The computational domain for the flow analyses includes an external far-field. NACA 1 series profile is adopted for the cowl-lip shape (NACA 1-854-35) [2]. The length from the end of the cowl-lip to the starting point of the S-shaped duct (constant sectional area region) is 2.169. The length of the remaining region (from the end point of the S-shaped duct to the outlet boundary) is 3.8.

$$z_{cl} = \Delta z_{cl}\left[1 - \cos\left(\pi\frac{x_{cl}}{L}\right)\right] \quad \text{(Centerline equation)} \qquad (22)$$

$$\left(\frac{R - R_i}{R_{ef} - R_i}\right) = 3\left(1 - \frac{x_{cl}}{L}\right)^4 - 4\left(1 - \frac{x_{cl}}{L}\right)^3 + 1$$

(Radius equation) $\qquad\qquad (23)$

with $R_i = 1.0$, $R_{ef} = 1.183$, $L = 7.1$, and $\Delta z_{cl} = 2.13$.

3.2. Grid system & boundary condition

A multi-block grid system is used to cover the flow field of the S-shaped diffuser including the external flow field. The size of the grid system is optimized through a grid refinement study. All the flow analysis and the design results in the present paper are based on a minimal grid size of 300,000 pts.
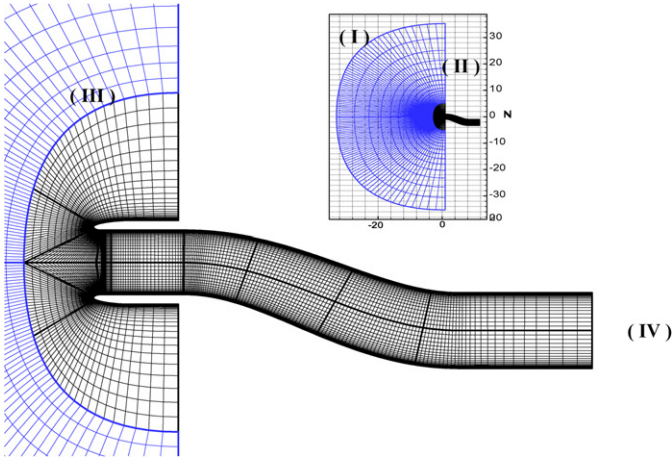
Fig. 4. Grid topology and boundary conditions for flow analysis of RAE2129 intake.

Fig. 4 shows the overall grid topology and boundary conditions. The first block covers the inner region from the cowl-lip to the engine face along the duct. The second block contains the remaining far-field region. The two blocks are subdivided again for parallel computing with domain decomposition.

A no-slip condition is applied explicitly along wall boundary and Riemann invariants are imposed on the far-field boundary I, II. Boundary III is the block interface. Along the duct centerline, a singular boundary condition is imposed by averaging the flow quantities of adjacent cells. At the engine face boundary (IV), a static pressure condition is given. The pressure value for each test case is given in [19].

3.3. Performance coefficients

The performance of the intake is measured by total pressure recovery and engine face distortion. Total pressure recovery, as shown in Eq. (24), is defined by the ratio of averaged total pressure at the engine face to that at the duct inlet section. Engine face distortion, as given in Eq. (25), represents flow non-uniformity at the engine face. All the centrifugal angles in Eq. (25) are evaluated at the outlet boundary section. In the design examples, the objective function is to diminish engine face distortion and to increase total pressure recovery while maintaining a mass flow rate condition.

$$\eta = \bar{p}_{0,ef}/\bar{p}_{0,in} \quad (ef: \text{engine face, } in: \text{inflow}), \tag{24}$$

$$DC(\phi) = \max\left[\bar{p}_0 - \bar{p}_0(\phi)\right]/\bar{q}, \tag{25}$$

where

$$\bar{p}_0 = \frac{\int_A p_0 \, dA}{\int_A dA}, \qquad \bar{p}_0(\phi) = \frac{\int_\phi p_0 \, dA}{\int_\phi dA}, \qquad \bar{q} = \frac{\int_A q \, dA}{\int_A dA},$$

and P_0 means total pressure, q is dynamic pressure. $\int_\phi$ indicates an integration over a angular domain as in Fig. 5, and $\int_A$ indicates an integration over the entire cross section area A. $DC(\phi)$ is the normalized maximum difference between $\bar{p}_0$ and $\bar{p}_0(\phi)$ for all possible angular domains.
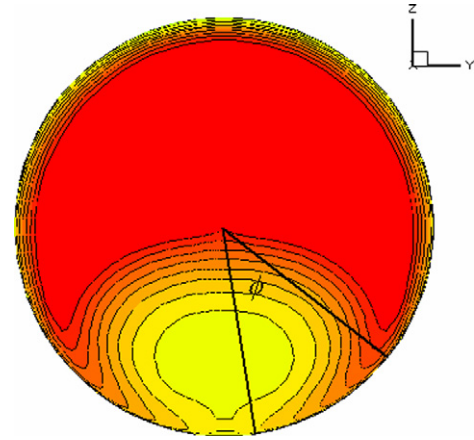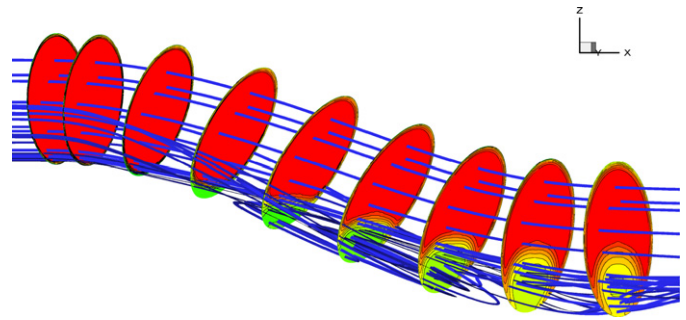

Fig. 5. Definition of engine face distortion.

Fig. 6. Total pressure contours and streamline pattern in the duct.

3.4. Validation of the flow solver

For the validation of the flow solver, the static surface pressure distributions are compared with the ARA (Aircraft Research Association) experimental data [17]. Main flow in the S-shaped intake can be characterized by separation on the starboard side and rotating incoming flow at the engine face as shown in Fig. 6. These phenomena are mainly affected by the flow expansion at the first bend of the S-shaped surface on the starboard side. These flow characteristics cause severe total pressure loss on the starboard side, which eventually produces unbalanced load on the fan of engine compressor and decreases intake efficiency. Thus, the accuracy of flow analysis depends on how well numerical methods and turbulence models can predict pressure distribution at the expansion region and separated flow on the starboard side.

On the starboard side (Figs. 3, 7), the pressure distribution shows good agreement with experimental data. By comparing several results with Spalart-Allmaras, $k-\omega$ and $k-\omega$ SST models by Menzies et al., it is shown that the $k-\omega$ SST model predicts the flow characteristics of the S-shaped duct better than other turbulence models, especially in inflow region and separation region where static pressure is almost constant [19]. Similarly, on the port side (Fig. 8), the result from $k-\omega$ SST matches the experimental data very well. Figs. 7, 8 show that the role of the turbulence model is very important to capture the flow characteristics in the S-shaped intake. As a direct consequence, the capability of the turbulence model to predict separation
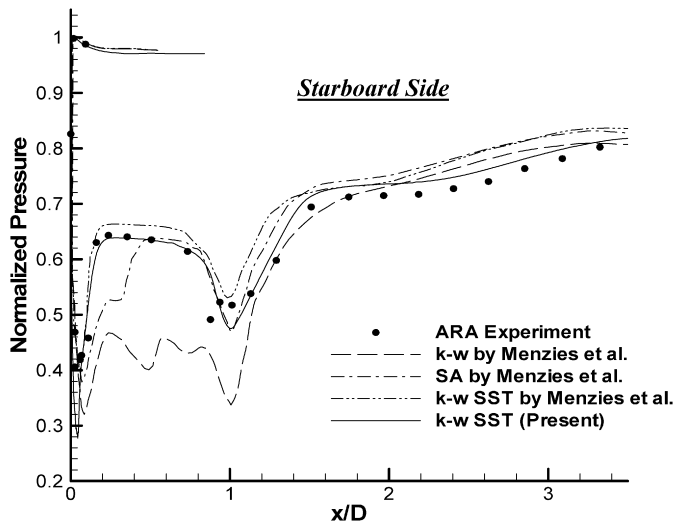
Fig. 7. Static pressure distribution along the star-board side and benchmarking cases.
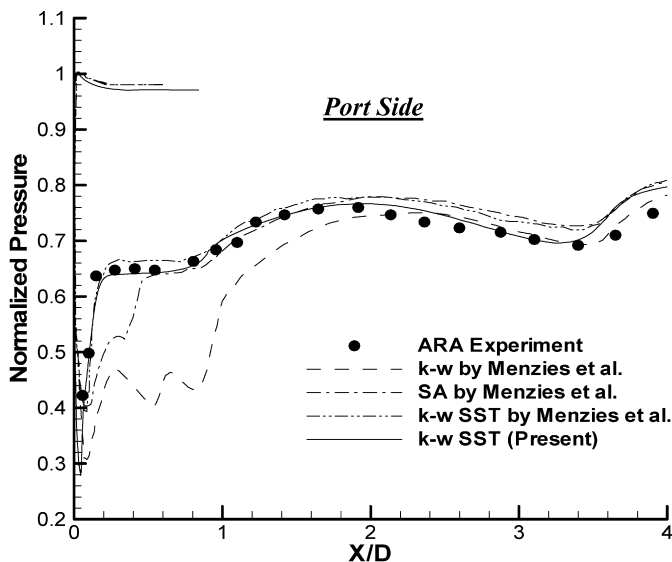

Fig. 8. Surface static pressure distributions along the port side and benchmarking cases.
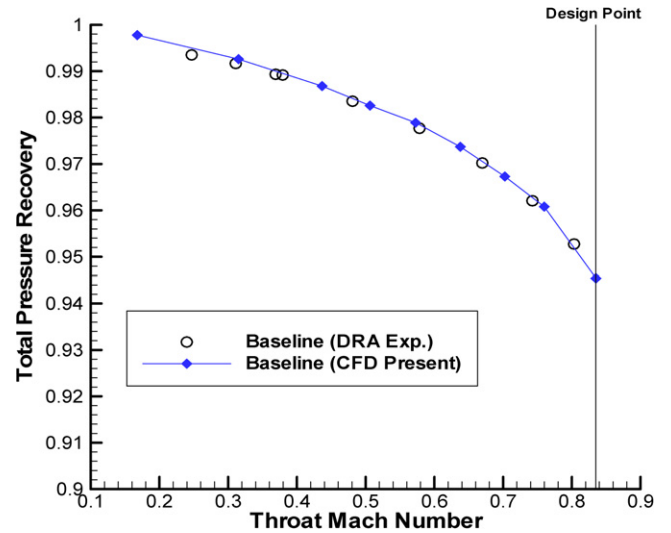

Fig. 9. Validation of flow solver – total pressure recovery in different throat Mach number conditions.
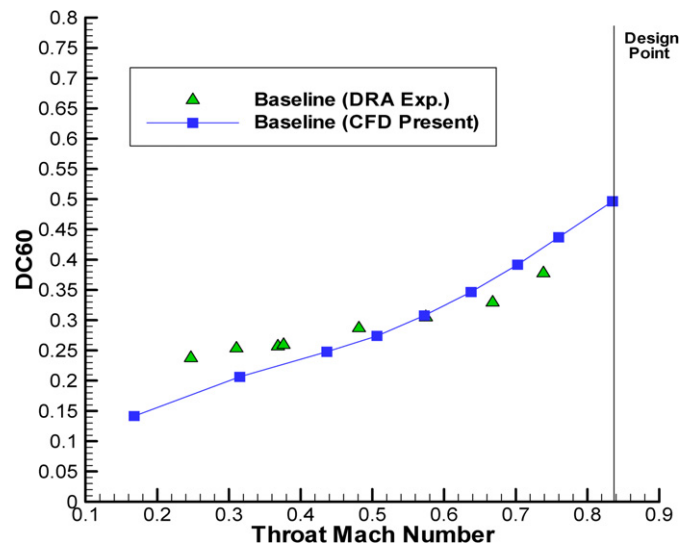
Fig. 10. Validation of flow solver – DC60 in different throat Mach number conditions.

accurately is critical in determining the sensitivity direction. Thus, the $k–\omega$ *SST* model is incorporated in the present flow and sensitivity analysis to better account for the turbulent effects.

For the benchmark of performance factors, the computed results in different throat Mach number conditions are compared with experimental data in Figs. 9 and 10. All the conditions in this figure are obtained by changing the back pressure. Even though the free-stream Mach number is merely 0.21, the throat Mach number reaches up to $M = 0.8$–0.9 for some back pressure conditions. For all throat Mach number conditions, the present solver yields very acceptable results in term of total pressure recovery and engine face distortion. The flow condition of the present design work belongs to a relatively high throat Mach number case where massive separated flow is observed.

4. Sensitivity analysis & design optimization

4.1. Validation of the sensitivity analysis

As mentioned above, the duct curvature is the main reason for the deterioration of intake performance. Thus, the surface geometry would be the most important design parameter and all the control points for the surface grid are adopted as design variables. Design parameters other than duct shape geometry are not considered: the sectional area of the duct inlet and outlet, and intake length are all fixed. 176 control points on the duct surface are used as design variables for the sensitivity analysis and the design process: 22 arrays of design variables along the centerline direction and 8 arrays along the circumferential direction as shown in Fig. 11. NURBS control points are then evaluated from the baseline grid, and the approximated NURBS function maintains the grid structure of baseline model com-
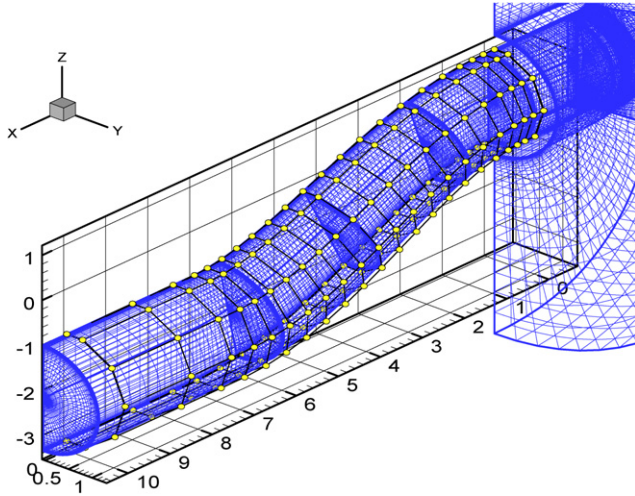
Fig. 11. Number and position of design variables.

pletely. As a result, sufficient design variables can be easily allocated to the region where flow phenomena are complex and grid density is high.

With regard to objective functions, the distortion coefficient and total pressure recovery are considered. By improving the geometric shape to minimize or maximize these performance factors, negative effects caused by flow separation are to be diminished. Gradients of the total pressure recovery and distortion for the centrifugal angle of 60° and 120° are adopted as objective functions for validation. Table 2 shows the comparison of several gradient values for each objective function with complex step derivatives. The step size for the complex step derivative is taken as 10^{-8} [16].

Sample design variables in Table 2 are selected at various positions. The expansion region on the starboard side (the 48th design variable) is checked and several different locations in the separation region are also examined (the 62nd, 78th, 108th, and 144th design variables). Each gradient value shows very good agreement with the complex step derivative results. Fig. 12 shows the contour of the adjoint variable Λ_1 for DC120. As each gradient value is determined by the product of grid sensitivity and adjoint variable, the sensitivity distribution can be assessed by adjoint variable contours. From the bottom view of Fig. 12, the expansion region looks highly sensitive and thus substantial geometric changes are expected in the design process.

4.2. Distortion minimization with constant mass flow rate

The design process should drive the initial geometry to an optimal shape without any loss in other performance measures. One of the major performance factors which should be conserved during the design process is the mass flow rate. Thus, for practical intake design, the mass flow rate should be considered. In the present design optimization case, the mass flow rate constraint is imposed in the form of penalty function as Eq. (26). Since both the number of constraints and the objective function affect the efficiency of the sensitivity analysis, the unconstrained optimization approach with an explicit penalty

Table 2
Validation of sensitivities

Design variable	48		62	
Method	AV	Complex	AV	Complex
PR	−8.4454E−2	−8.4463E−2	−7.3632E−4	−7.3605E−4
DC60	−6.7802E−3	−6.7815E−3	−1.2262E−4	−1.2262E−4
DC120	−1.8059E−1	−1.8064E−1	−7.2732E−2	−7.2700E−2
Design variable	74		108	
Method	AV	Complex	AV	Complex
PR	6.5328E−4	6.5324E−4	−3.6324E−3	−3.6342E−3
DC60	2.1670E−2	2.1654E−2	−2.2446E−2	−2.2467E−2
DC120	−1.3268E−3	−1.3266E−3	4.5722E−2	4.5742E−2
Design variable	144		166	
Method	AV	Complex	AV	Complex
PR	−2.4329E−3	−2.4329E−3	7.0511E−3	7.0499E−3
DC60	3.0338E−1	3.0284E−1	2.4144E−2	2.4135E−2
DC120	2.5727E−1	2.5728E−1	−5.3619E−2	−5.3624E−2

Adjoint Variable Contour(G1) for DC120
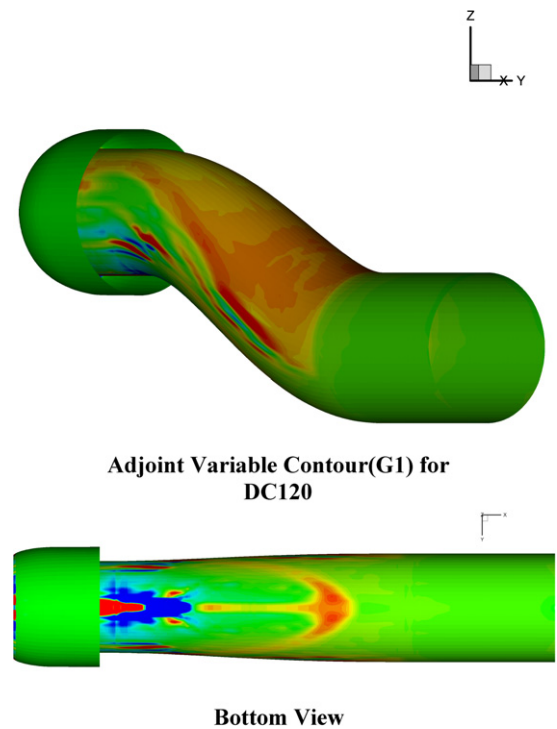
Bottom View

Fig. 12. Adjoint variables of the continuity equation for DC120.

function is adopted in the DC minimization.

$$F = DC(\theta) + Wt \times \text{Max}(0, \dot{m}_0 - \dot{m}) \quad (\dot{m}_0 = 1.78). \quad (26)$$

Weighting factor Wt is given by the $L2$ norm ratio of initial sensitivities as in Eq. (27).

$$Wt = \left\| \left\{ \frac{dDC(\theta)}{d\beta_k} \right\} \right\| \Big/ \left\| \left\{ \frac{d(\dot{m})}{d\beta_k} \right\} \right\|. \quad (27)$$

The first term of the objective function, DC120, decreases from 0.3367 to 0.2519 in the designed model. The total pressure recovery increases from 0.9453 to 0.9574. It is noted that
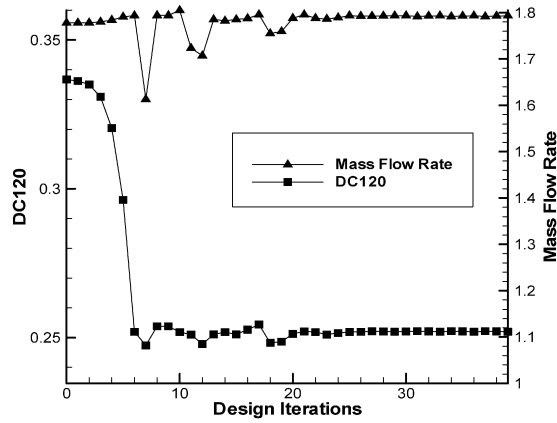
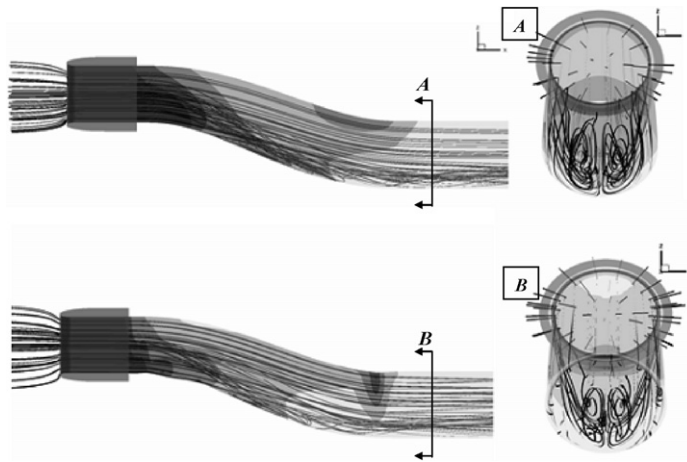Fig. 13. Convergence history of design procedure (DC minimization with constant MFR).

Fig. 14. Shape and streamlines comparison (DC minimization with constant MFR, U: baseline, L: designed).

the mass flow rate is maintained at 1.779 which is almost equal to the initial mass flow rate. Fig. 13 shows the convergence history of the overall optimization procedure. It is shown that the design process satisfies the constraint imposed by the initial mass flow rate. Fig. 14 compares the change of shape and flow pattern before and after the design. Curvature at the first curved region decreases and a small bump is formed, which alleviates rapid flow acceleration on the lower surface. As a result, the expansion region is substantially reduced and flow separation is delayed. Similarly, the streamline pattern clearly shows the enhancement of flow quality.

4.3. Volume-averaged total pressure (VATP) maximization

The main aim of the present section is to maximize the total pressure recovery without any loss in other performance measures. Thus, overall flow quality in the whole duct should be reflected upon by the objective function. In this sense, the maximization of volume-averaged total pressure (VATP) is adopted as a useful objective function. VATP is defined by Eq. (28).

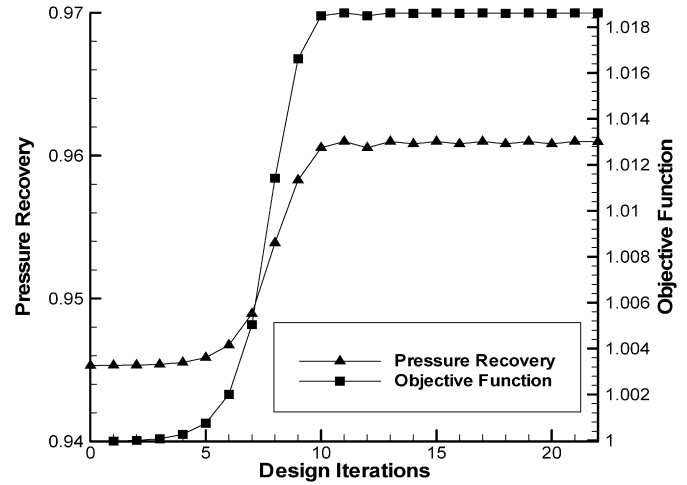$$\text{VATP} = \int_V P_0 \, dv \bigg/ \int_V dv, \tag{28}$$

Fig. 15. Convergence history of design procedure (VATP maximization).

where $\int_V$ implies the volume integration from $x/D = 0$ (D: throat diameter) to the outlet boundary.

Fig. 15 shows the convergence characteristic of the overall design procedure. As shown in the figure, the normalized VATP increases from 1.00 to 1.018. Although the change of the objective function looks very small, the total pressure recovery increases substantially from 0.9453 to 0.9610. The 1.5% change of the total pressure recovery implies a significant improvement considering that engine thrust is directly proportional to the total pressure recovery at the engine intake [22]. Flow distortions are decreased by 3–7%. Fig. 16 shows the geometric change between the baseline model and the designed model. The duct geometry after the design is somewhat beyond expectation, and it appears that this kind of shape change can rarely be obtained from conventional design works. Intuitively, three noticeable features can be observed from Figs. 16, 17. The first feature is that the first curved region at the lower surface is stretched after the design. Due to this change, the suction effect at the lower surface becomes weak and the size of the flow separation is reduced remarkably. This geometric change is similar to the result of the previous design case. However, two other geometric changes are distinguishable. One is that the exhaust region of the designed intake is transformed into an elliptical shape from a circular section of the baseline model. This decreases the intensity of swirling flow over the whole duct region. The other is a smooth bump along the lower surface near the exhaust region, which actually stabilizes flow into the engine face. For a more detailed comparison, the static pressure distribution on the starboard side and the sectional area distribution are presented in Fig. 18. It is noted that the sectional area in front of the starting position of the S-curved region, where an excessive expansion is generated in the baseline model, increases. As can be seen from static pressure distribution, this geometric change produces an efficient diffuser effect to make the flow velocity decrease rapidly. Therefore, thanks to the deceleration of the flow, the size of the separation (constant static pressure region) is reduced considerably and pressure increases mildly over the whole region of the S-curved region. In the exhaust region, which is near the smooth bump region, a negative pressure
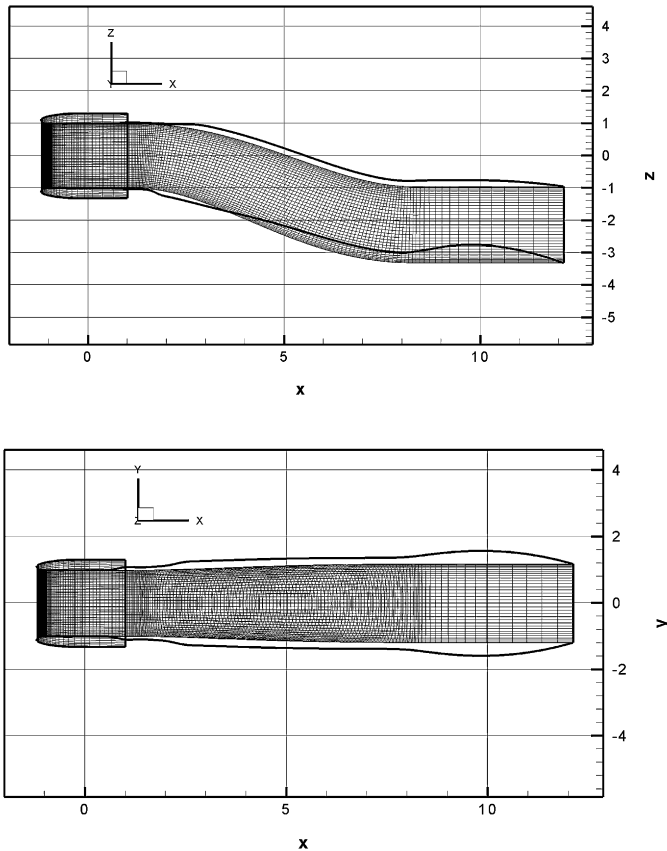
Fig. 16. Comparison of duct shape (VATP maximization, mesh: baseline, outline: designed).
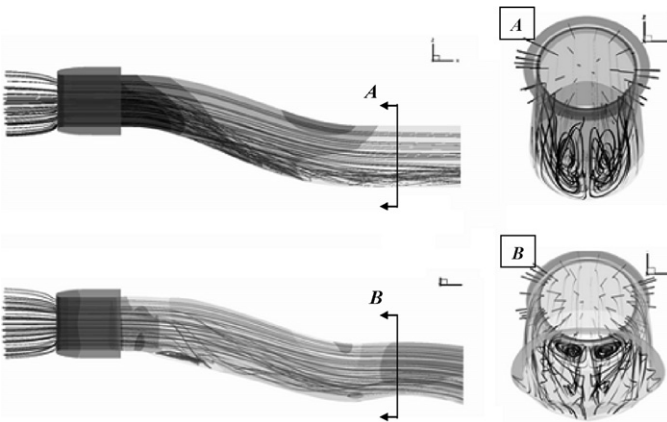

Fig. 17. Streamline comparison (VATP maximization, U: baseline, L: designed).

gradient is generated. As a result, the bump helps to stabilize the flow and to provide more uniform flow into the engine face. These kinds of geometric changes can avoid non-uniform aerodynamic load to engine compressor and efficiently reduce total pressure loss.

4.4. Off-design condition test for designed case

Based on the results of the VATP maximization, the performance of the designed model is examined at several off-design
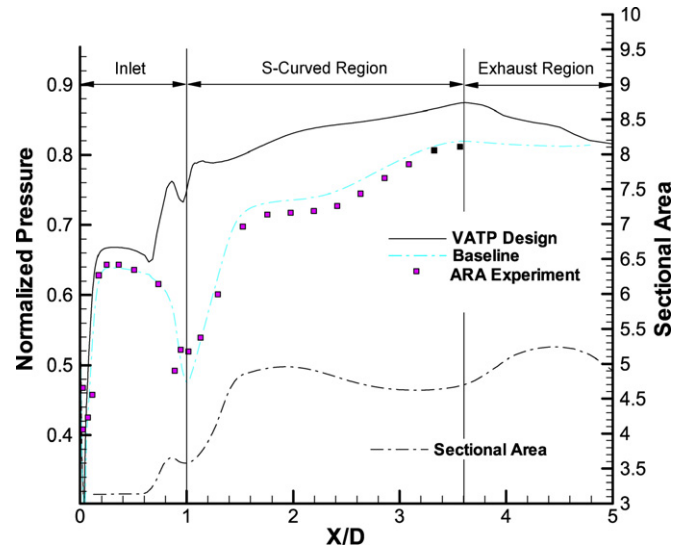

Fig. 18. Comparison of static pressure and sectional area distribution of designed model (VATP maximization).

Table 3
Off-design condition test

Conditions	Model	PR	MFR	DC60	DC90
$M = 0.21$	Baseline	0.9453	1.7788	0.4964	0.4236
AOA $= 0°$	Designed	0.9610	1.7607	0.4637	0.4131
$M = 0.3$	Baseline	0.9340	1.8550	0.7629	0.6847
AOA $= 0°$	Designed	0.9483	1.8592	0.6811	0.6425
$M = 0.4$	Baseline	0.9036	1.9468	0.8560	0.7864
AOA $= 0°$	Designed	0.9199	1.9564	0.6395	0.6078

conditions. The performance coefficients of baseline and designed geometry are compared by changing the free-stream Mach number. Results for the three different free-stream Mach numbers ($M_\infty = 0.21, 0.3, 0.4$) are presented in Table 3. For each design case, total pressure recovery, distortion and mass flow rate are compared under the same free stream conditions and back pressure condition. It can be seen that the designed model shows a better performance than the baseline model in all the off-design test cases. As the mass flow rate condition changes, the total pressure recovery of the designed model shows again overall improved performance in Fig. 19.

Through design and off-design condition tests, the present design optimization approach using an adjoint code and NURBS shape modification tool successfully demonstrates that the designed model exhibits a good performance in various flight conditions. Even if it may not guarantee the globally optimal shape, several tests at off-design conditions confirm that the designed model yields very desirable performance over a wide range of flow conditions.

5. Conclusion

Based on the adjoint approach with a NURBS shape modification function, the global shape improvement of an S-shaped subsonic intake is carried out. For an efficient and accurate design procedure, a high fidelity sensitivity analysis code, grid generator and optimization programs are developed through the
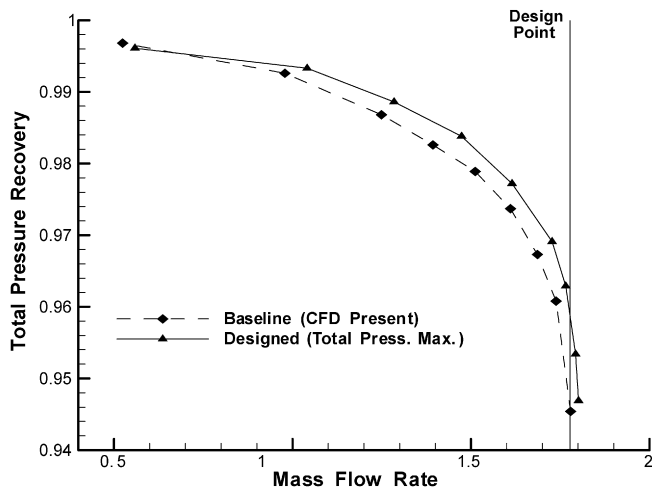
Fig. 19. Performance test of designed model according to mass flow rate conditions.

present work. Key flow physics of the S-shaped diffuser such as strong vortex and flow separation could be captured by applying a two-equation turbulence model. Especially, $k-\omega$ *SST* model yields good results compared to other 1 or 2-Eq. turbulence models, and computed results are not so sensitive to grid refinement. With regard to the sensitivity analysis, the turbulence effect is incorporated accurately by hand-differentiating the two-equation turbulence model using the discrete adjoint approach. The NURBS control points obtained by a NURBS least-square approximation are used as design variables to modify the duct geometry. Using about 180 design variables, sufficient design space for flexible geometric change could be obtained. From the present design works and off-design condition tests, the capability and the efficiency of the present design methodology based on the adjoint approach and NURBS shape functions is successfully demonstrated in three-dimensional turbulent internal flow analysis and design optimization. Thus the present design methodology can be applied not only to general subsonic/transonic duct design problem but also to more detailed design works of flow control devices such as vortex generating vanes or vortex generating jets.

Acknowledgements

References

[1] B.H. Anderson, J. Gibb, Vortex-generator installation studies on steady-state and dynamic distortion, J. Aircraft 35 (4) (1998) 513–520.

[2] D.D. Baals, N.F. Smith, J.B. Wright, The development and application of high-critical-speed nose inlets, NACA Report 920.

[3] J. Brezillon, N.R. Gauger, 2D and 3D aerodynamic optimization using the adjoint approach, Aerospace Science and Technology 8 (8) (2004) 715–722.

[4] G. Carrier, Single and multipoint aerodynamic optimization of a supersonic transport aircraft wing using optimization strategies involving adjoint method and genetic algorithm, ONERA TP 2006-61.

[5] Fluid Dynamics Panel – Working Group 13, Test Case 3 – subsonic/transonic circular intake, AGARD Advisory Report 270, 1991.

[6] G.J. Harloff, B.A. Reichert, S.R. Wellborn, Navier–Stokes analysis and experimental data comparison of compressible flow in a diffusing S-duct, AIAA 92-2699.

[7] R.M. Hicks, P.A. Henne, Wing design by numerical optimization, J. Aircraft 15 (7) (1978) 407–412.

[8] A. Jameson, S. Kim, Reduction of the adjoint gradient formula for aerodynamic shape optimization problems, AIAA J. 41 (11) (2003) 2114–2129.

[9] C.S. Kim, C. Kim, O. Rho, Sensitivity analysis for the Navier–Stokes equations with two-equation turbulence models, AIAA J. 39 (5) (2001) 838–845.

[10] S. Kim, C. Kim, O. Rho, S. Hong, Cures for the shock instability: development of shock-stable roe schemes, J. Computational Physics 185 (2) (2003) 342–374.

[11] S. Koc, H. Kim, K. Nakahashi, Aerodynamic design optimization of wing-body configurations, AIAA 2005-331.

[12] K.W. Lee, Principles of CAD/CAM/CAE Systems, Addison Wesley, 1998.

[13] B.J. Lee, C.S. Kim, C. Kim, O. Rho, K.D. Lee, Parallelized design optimization for transonic wing using aerodynamic sensitivity analysis, AIAA 2002-0264.

[14] B.J. Lee, C. Kim, O. Rho, Optimal shape design of the S-shaped subsonic intake using NURBS, AIAA 2005-0455.

[15] K. Leoviriyakit, S. Kim, A. Jameson, Viscous aerodynamic shape design optimization of wings including planform variables, AIAA 2003-3498.

[16] J.R.R.A. Martins, I.M. Kroo, J. Alonso, An automated method for sensitivity analysis using complex variables, AIAA 2000-0689.

[17] N.E. May, C.J. Peace, C.A. Mchugh, An investigation of two intake/S-bend diffuser geometries using the sauna CFD system – phase 1, ARA Memo 386, 1993.

[18] F.R. Menter, Two-equation eddy-viscosity turbulence models for engineering applications, AIAA J. 32 (8) (1994) 1598–1605.

[19] R.D.D. Menzies, K.J. Badcock, G.N. Barakos, B.E. Richards, Validation of the simulation of flow in an S-duct, AIAA 2002-2808.

[20] E.J. Nielsen, W.K. Anderson, Aerodynamic design optimization on unstructured meshes using the Navier–Stokes equations, AIAA 98-4809.

[21] L. Piegl, W. Tiller, The NURBS Book, Springer, 1997.

[22] J. Seddon, E.L. Goldsmith, Intake Aerodynamics, AIAA Education Series, AIAA, 1985.

[23] C.F. Smith, J.E. Bruns, G.J. Harloff, J.R. DeBonis, Three-dimensional compressible turbulent computations for a diffusing S-duct, NASA CR 4392, 1991.

[24] R.K. Sullerey, S. Mishra, A.M. Pradeep, Application of boundary layer fences and vortex generators in improving performance of S-duct diffuser, J. Fluids Engineering 124 (2002) 136–142.

[25] E.S. Taskinoglu, D.D. Knight, Design optimization for submerged inlets – part II, AIAA 2003-3926.

[26] S.R. Wellborn, B.A. Reichert, T.H. Okiishi, Experimental investigation of the flow in a diffusing S-duct, AIAA 92-3622.

[27] S. Yoon, D. Kwak, Three-dimensional incompressible Navier–Stokes solver using lower-upper symmetric-Gauss–Seidel algorithm, AIAA J. 29 (1991) 874–875.

[28] W. Zhang, D. Knight, D. Smith, Automated design of a three-dimensional subsonic diffuser, J. Propulsion and Power 16 (6) (2000) 1132–1140.